CHINESE OPTICS LETTERS
Vol. 19, No. 6 | June 2021

High-Q lithium niobate microring resonators using lift-off metallic masks [Invited]

Ke Zhang (张 珂)[1,†], Zhaoxi Chen (陈朝夕)[1,†], Hanke Feng (冯寒珂)[1], Wing-Han Wong (黄咏娴)[1], Edwin Yue-Bun Pun (潘裕斌)[1,2], and Cheng Wang (王 骋)[1,2*]
[1] Department of Electrical Engineering, City University of Hong Kong, Kowloon, Hong Kong, China
[2] State Key Laboratory of Terahertz and Millimeter Waves, City University of Hong Kong, Kowloon, Hong Kong, China

*Corresponding author: cwang257@cityu.edu.hk
Received March 7, 2021 | Accepted April 7, 2021 | Posted Online May 8, 2021

High-Q lithium niobate (LN) optical micro-resonators are an excellent platform for future applications in optical communications, nonlinear optics, and quantum optics. To date, high-Q factors are typically achieved in LN using either dielectric masks or femtosecond laser ablation, while the more standard and commonly available lift-off metallic masks are often believed to lead to rough sidewalls and lowered Q factors. Here, we show that LN microring resonators with strong light confinement and intrinsic Q factors over 1 million can be fabricated using optimized lift-off metallic masks and dry etching processes, corresponding to a waveguide propagation loss of $\sim$0.3 dB/cm. The entire process is fully compatible with wafer-scale production and could be transferred to other photonic materials.

Keywords: lithium niobate; optical resonators; microstructure fabrication.
DOI: 10.3788/COL202119.060010

1. Introduction

Lithium niobate ($LiNbO_3$, LN) is an excellent photonic material for integrated optics, owing to its unique linear and nonlinear optical properties, including high refractive index, large second-order nonlinear susceptibility ($\chi^{(2)} = 27$ pm/V), and wide optical transparency window (400 nm to 5 μm)[1,2]. In traditional bulk LN devices, optical waveguides are mainly defined by titanium (Ti)-diffusion or proton-exchange methods with low refractive index contrasts. Recent years have witnessed the rapid development of LN-on-insulator (LNOI) technology, where a sub-micron thick LN thin film is bonded on top of a silica (SiO_2) substrate, leading to an index contrast of ~0.7, much better optical confinement, and substantially improved device performances[3–22]. In particular, the achievement of high-Q optical micro-resonators in the LNOI platform, including microring resonators[9], microdisk resonators[10,11], and photonic crystal cavities[12], has allowed a variety of nonlinear optical and electro-optic devices with unprecedented functionalities and performances, such as ultra-efficient nonlinear wavelength convertors[13,14], broadband electro-optic/Kerr frequency comb sources[15–17], quantum microwave-to-photon convertors[18,19], efficient acousto-optic modulators[20,21], as well as unidirectional frequency shifters[22].

To date, the majority of high-Q ($> 10^6$) LNOI micro-resonators have been realized by dry etching using dielectric etching masks such as Si[23], SiO_2[24], or hard electron-beam resists like hydrogen silsesquioxane (HSQ)[9] and ZEP[17]. Although these mask materials typically yield low selectivity of $< 1:1$ in the argon ion (Ar^+)-based dry etching process, they have successfully been used to produce smooth waveguide sidewalls and resonators with Q factors as high as 10^7[9]. An alternative approach is based on chromium (Cr) masks fabricated by femtosecond laser machining, followed by a chemical–mechanical polishing (CMP) process to form smooth wedge-like structures in the LN thin film[25], which has led to Q factors close to the material absorption limit of LN ($\sim 10^8$)[26]. These methods, however, often involve special processes or chemicals (e.g., HSQ) that are not readily available in every lab. The low etching selectivity and small wedge angle could also pose challenges in creating deep sub-wavelength photonic structures. In contrast, the more standard and commonly available metallic masks, typically prepared using lithography and lift-off processes, have not been widely used for low-loss LN integrated photonics. It is commonly perceived that lift-off metallic masks inevitably lead to rough sidewalls and large scattering losses.

The origins for exacerbated roughness in lift-off metallic masks are mainly two-fold. First, an unoptimized lithography process could cause mask fencing or even bridging at the lift-off edges, if the resist is not carefully tailored to have the desired undercut profile[27]. Second, metallic materials deposited by sputtering or evaporation naturally form grains on the scale

of tens of nanometers, ultimately limiting the edge smoothness of these metallic masks. As a result, LNOI micro-resonators fabricated using lift-off metallic masks and dry etching typically exhibit Q factors in the 10^5 range[28–30]. While excessive post-etching surface polishing has been shown to further improve the Q factors by an order of magnitude[29], the demonstration has been limited to donut-like structures with widths of ~8 μm, which are not compatible for applications that require tight optical confinement and/or dispersion engineering.

In this article, we show that, contrary to common beliefs, standard lift-off metallic masks can well produce LNOI micro-resonators with Q factors over 1 million. By carefully engineering the lift-off resist profile and dry etching process, we demonstrate microring resonators with a measured loaded (intrinsic) Q factor of $\sim 5.5 \times 10^5$ (1.1×10^6), corresponding to a waveguide propagation loss of ~0.3 dB/cm.

2. Methods

The waveguide-coupled microring resonators are fabricated from a commercially available x-cut LNOI wafer (NANOLN). The wafer stack consists of a 600 nm LN thin film, a 4.7 μm buried SiO_2 layer, and a 500 μm silicon substrate, as shown in Fig. 1(a). Electron-beam lithography (EBL) is first used to pattern the bus waveguides and microrings in poly-methyl methacrylate (PMMA) resist, as illustrated in Fig. 1(b). The resist patterns are then transferred to a 180 nm nichrome (NiCr) mask layer through thermal evaporation [Fig. 1(c)] and a standard lift-off process in acetone [Fig. 1(d)]. The mask patterns are subsequently transferred to the LN layer by an optimized Ar^+-based reactive ion etching (RIE) process, as shown in Fig. 1(e). The Ar^+ ions physically bombard the exposed LN film with a radio-frequency power of ~250 W and a bias voltage of ~530 V, resulting in an etching selectivity of approximately 2:1. The etching selectivity is significantly higher than that of common dielectric masks and could be beneficial in creating deep sub-wavelength structures. After the residual NiCr mask is removed in Cr etchant [Fig. 1(f)], an optional CMP process could be applied on the sample surface to further reduce the surface roughness[29]. Here, we only apply a soft 4×10^4 min · Pa polishing step, which does not significantly change the device Q factors (< 20%) according to Ref. [29] and our own experiences.

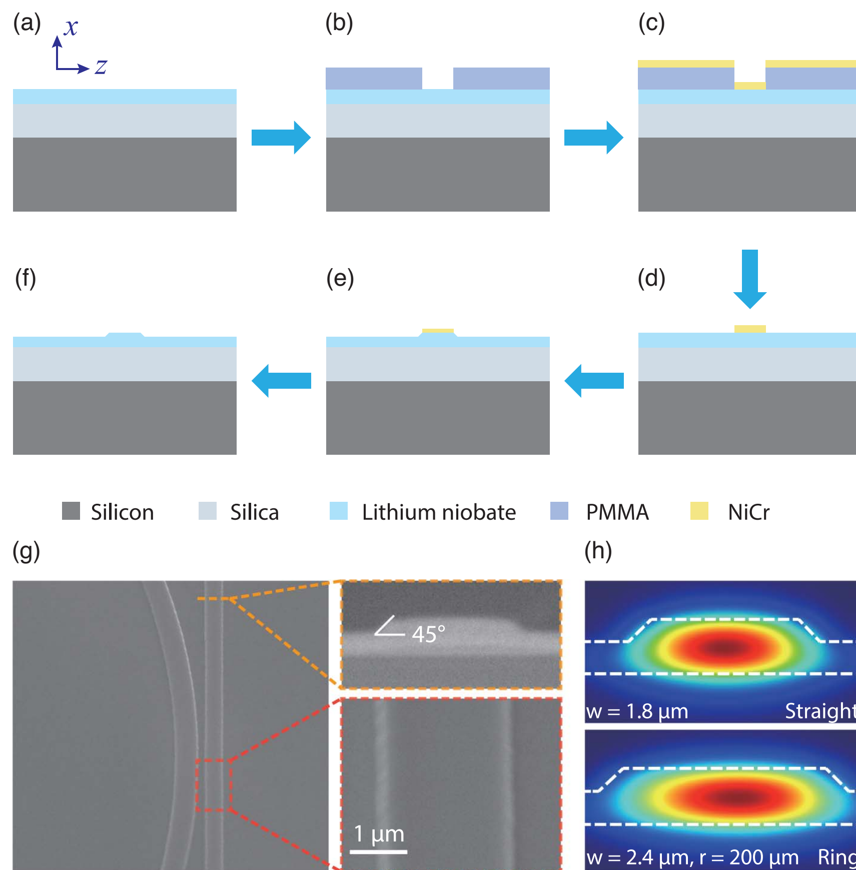

Fig. 1. (a)–(f) Device fabrication flowchart. (a) Fabrication starts with an x-cut LNOI substrate. (b) PMMA resist is first spin-coated and patterned with EBL. (c) NiCr etching mask is subsequently created by thermal evaporation, (d) followed by a standard lift-off process. (e) The patterned NiCr is then used as an etching mask to form the LN waveguides using an Ar^+-based RIE process. (f) The residual NiCr is finally removed in Cr etchant. (g) SEM images of a fabricated microring resonator and a coupling bus waveguide. Insets show magnified cross-section (top) and top-down (bottom) views of the bus waveguide. (h) Simulated electric field (E_z) profiles of the fundamental TE modes in the straight bus waveguide (top) and the bending ring waveguide (bottom).

Instead, we focus on the investigation and optimization of the lift-off mask quality for better device performance in this paper. Finally, the chip facets are cleaved for end-fire coupling.

Figure 1(g) shows the scanning electron microscope (SEM) images of a fabricated microring resonator with a radius of 200 μm and a coupling waveguide. The rib-like waveguides feature a rib height of 240 nm, an unetched slab thickness of 340 nm, and a sidewall angle of ~45° [Fig. 1(g)]. The top widths of the bus waveguides and the rings are 1.8 μm and 2.4 μm, respectively. These micron-scale waveguides provide strong optical confinement and possibilities for dispersion engineering in the telecommunication bands. Figure 1(h) shows the simulated electric field (E_z) distributions of the fundamental transverse-electric (TE) modes for both the bus waveguide (top) and the ring waveguide (bottom). For the ring waveguide simulation, the bending radius of 200 μm has been taken into account, resulting in the slightly asymmetric mode distribution.

3. Results and Discussions

By performing step-by-step SEM examinations of the device cross-section profiles (Fig. 2), we show that the roughness in the lift-off metallic masks mainly originates from non-ideal resist profiles and can be largely eliminated by optimizing the lithography and lift-off processes. The left column of Fig. 2 shows the PMMA and NiCr profiles during a typical, unoptimized lift-off mask preparation process. The cross-section SEM images are taken by cleaving the chip in the direction perpendicular to the waveguides after each step. The SEM images show different structures, since they are taken from different areas of the chip due to uncertainties in hand cleavage positions. Nevertheless, the images shown in each column are from the same chip and still provide important insights for optimizing the lift-off processes step by step. We find that although the PMMA profile right after EBL looks almost perfectly vertical [Fig. 2(a)], it often experiences substantial deformation during the thermal evaporation process, which in turn leads to an overcut resist profile [Fig. 2(c)]. As a result, NiCr is deposited not only at the bottom surface, but also on the resist sidewalls, which ultimately translates into fencing features on the final lift-off masks [Fig. 2(e), showing top-down view]. Such features are typically hundreds of nanometers in size and will be directly transferred into the sidewall roughness of the final LN devices.

We show that the rough features on the NiCr masks can be significantly reduced by optimizing each fabrication step in the lift-off process, as shown in the right column of Fig. 2. First, we create an undercut PMMA resist profile by fine tuning the PMMA film thickness, EBL exposure energy, and development time [Fig. 2(b)]. For the micron-scale waveguides shown in this paper, we use a 1.3 μm thick PMMA layer (950 A11), with an EBL dose of 1000 μC/cm^2 and 20 s development time in a

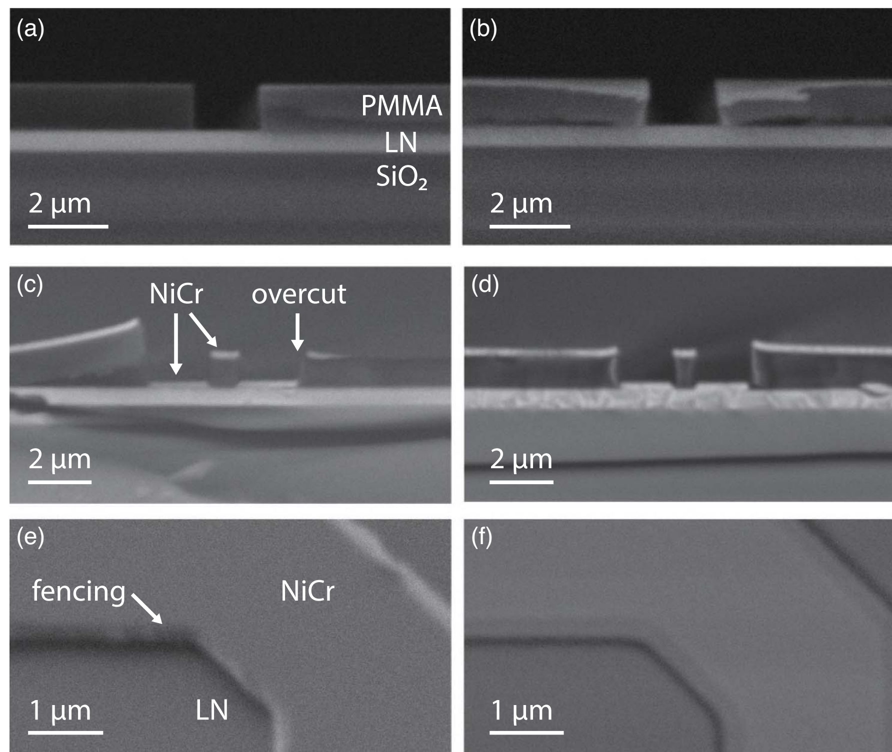

Fig. 2. Step-by-step SEM examinations of the lift-off processes. (a), (b) Cross-section profiles of the PMMA resist after EBL. (c), (d) Cross-section profiles after thermal evaporation. (e), (f) Top-down views of the final NiCr masks. The left column [(a), (c), and (e)] shows a typical unoptimized lift-off process with overcut resist profiles and mask fencing features, whereas the right column [(b), (d), and (f)] corresponds to the optimized process with smooth mask profiles. The left part of PMMA resist in (c) was accidentally detached from the substrate during the cleaving step.

methyl isobutyl ketone/isopropyl alcohol (MIBK/IPA) 1:3 solution. We then optimize the NiCr mask material quality (i.e., grain size) by evaporation at relatively low rates (1–2 Å/s, 1 Å = 0.1 nm) and low pressure. We also limit the time for each continuous evaporation step to <15 min to minimize thermal deformation of PMMA. As a result, the desired undercut resist profile is well maintained after metal deposition, as shown in Fig. 2(d). The final lift-off NiCr mask shows smooth sidewalls without fencing features [Fig. 2(f)], which lays the foundation for our high-Q micro-resonators. The slightly slanted NiCr sidewalls in Fig. 2(f) are likely results of non-vertical thermal evaporation with respect to the substrate. In our experience, these slanted masks do not significantly affect the final device sidewall roughness, but could be a reason for the smaller etched LN sidewall angle (~45°) compared with those commonly achieved using HSQ masks (~70°)[15]. Using these optimized NiCr masks for the subsequent dry etching step, we achieve LN photonic devices with relatively smooth etched sidewalls, as shown in Fig. 1(g). The zoom-in view of these etched structures still reveals observable roughness, which is likely induced by the remaining metal grain boundaries. The surface roughness of these devices could be further reduced by applying a longer post-etching CMP process, which has been thoroughly studied in Ref. [29] and is beyond the focus of this paper.

We characterize the Q factors of the fabricated LNOI microring resonators using an end-fire coupling system shown in Fig. 3(a). Continuous-wave (CW) light from a tunable telecom laser (Santec TSL-550) is coupled into the input facet of the bus waveguide using a lensed fiber. The output signal is collected by a second lensed fiber and monitored using a photodetector (PD). Figures 3(b)–3(e) show the measured optical transmission spectra of LNOI microring resonators fabricated using unoptimized (left column) and optimized (right column) lift-off metallic masks. The two microrings have different radii of 100 μm and 200 μm resulting in free spectral ranges (FSRs) of 1.7 nm [Fig. 3(b)] and 0.85 nm [Fig. 3(c)], respectively, which do not affect our discussions on Q factors in these roughness-limited resonators. Figures 3(d)–3(e) show the zoom-in views of critically coupled resonance dips for the two processes, along with their Lorentzian fits (red curve). For the unoptimized process

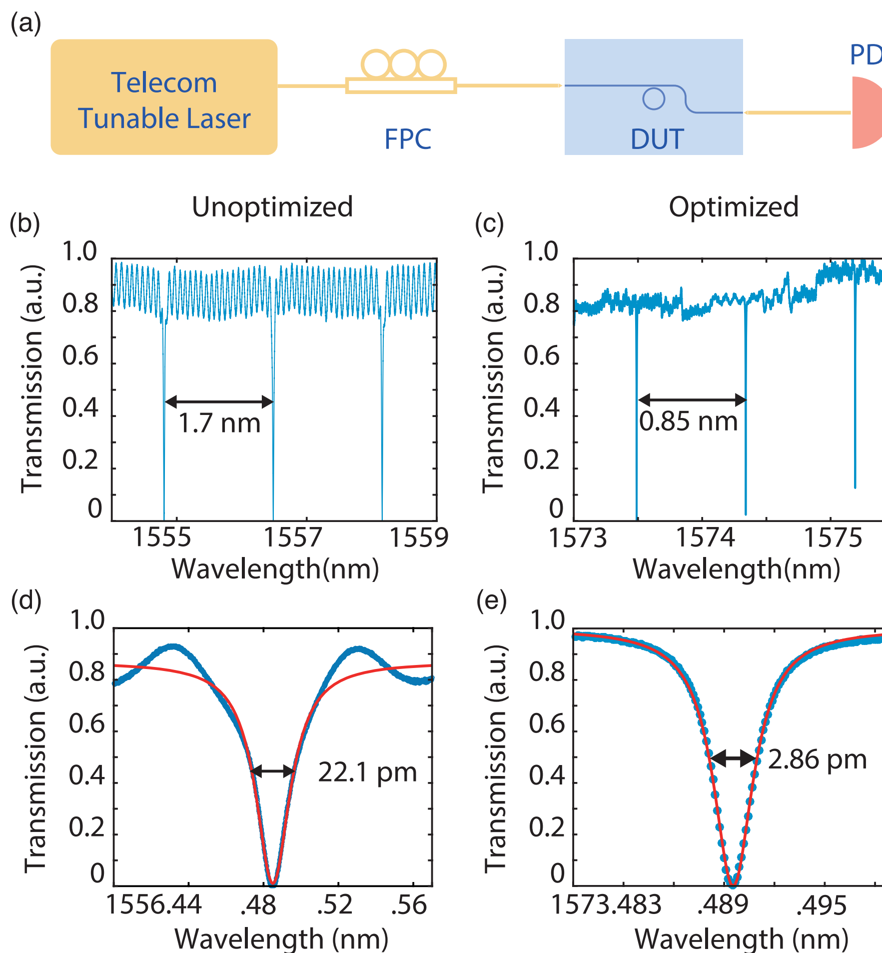

Fig. 3. (a) Experimental setup for LN microring resonator characterization. FPC, fiber polarization controller; DUT, device under test; PD, photodetector. Measured optical transmission spectra for typical microring resonators using (b) unoptimized and (c) optimized fabrication processes. (d) and (e) Zoom-in views of (b) and (c) showing critically coupled resonances. Blue dots show the measured data, and red curves correspond to the Lorentzian fits, indicating intrinsic Q factors of 1.4×10^5 and 1.1×10^6 for unoptimized and optimized metallic masks, respectively.

[Fig. 3(d)], the fitted curve reveals a resonance linewidth of 22.1 pm, corresponding to a relatively low loaded (intrinsic) Q factor of 7.0×10^4 (1.4×10^5). In contrast, using our optimized NiCr mask and dry etching process, we achieve microring resonators with a measured intrinsic Q factor over 1 million. As shown in Fig. 3(e), we measure a critically coupled resonance linewidth of 2.86 pm at 1573.5 nm, which corresponds to a loaded Q factor of 5.5×10^5 and an intrinsic Q factor of 1.1×10^6, almost an order of magnitude higher than that achieved using the unoptimized process. From the measured Q factors, we can also estimate the waveguide propagation losses to be $\sim$0.3 dB/cm. These million-level Q factors, although not as high as some recent LNOI demonstrations[9,10], could already serve the purpose for a majority of LNOI applications and are achieved using standard lift-off metallic masks and wafer-compatible processes. The wavelength-scale photonic structures are ideally suited for dispersion engineering in nonlinear optics and electrode patterning in electro-optic applications. The Q factors can be further improved by applying a longer CMP process[29], as well as cladding the devices in SiO_2 to reduce the index contrast across the etched surface.

4. Conclusions

In conclusion, we have demonstrated LN microring resonators with intrinsic Q factors over 1 million using standard lift-off metallic masks and dry etching. We show that commonly observed non-ideal features in lift-off masks can be largely eliminated by optimizing the lithography, evaporation, and lift-off processes, leading to smooth etched surfaces and Q factors comparable with other popular LNOI fabrication techniques. Compared with masks based on dielectrics or hard electron-beam resists, these more standard and commonly available metallic masks exhibit substantially higher etching selectivity ($\sim$2∶1) and could provide opportunities in creating deep sub-wavelength LNOI photonic structures such as metasurfaces or inverse-designed devices. The entire process is fully compatible with wafer-scale production and could also be transferred to other difficult-to-process photonic materials like TiO_2 and SiC.

Acknowledgement

We thank Dr. Wenzhao Sun for helpful discussions. This work was supported by the National Natural Science Foundation of China (No. 61922092), Research Grants Council, University Grants Committee (No. CityU 21208219), and City University of Hong Kong (Nos. 9667182, 9610402, and 9610455).

†These authors contributed equally to this work.

References

1. L. Arizmendi, "Photonic applications of lithium niobate crystals," Phys. Status Solidi **201**, 253 (2004).
2. A. Boes, B. Corcoran, L. Chang, J. Bowers, and A. Mitchell, "Status and potential of lithium niobate on insulator (LNOI) for photonic integrated circuits," Laser Photon. Rev. **12**, 1700256 (2018).
3. J. Lin, F. Bo, Y. Cheng, and J. Xu, "Advances in on-chip photonic devices based on lithium niobate on insulator," Photon. Res. **8**, 1910 (2020).
4. A. Rao and S. Fathpour, "Heterogeneous thin-film lithium niobate integrated photonics for electrooptics and nonlinear optics," IEEE J. Sel. Top. Quantum Electron. **24**, 8200912 (2018).
5. C. Wang, M. Zhang, X. Chen, M. Bertrand, A. Shams-Ansari, S. Chandrasekhar, P. Winzer, and M. Lončar, "Integrated lithium niobate electro-optic modulators operating at CMOS-compatible voltages," Nature **562**, 101 (2018).
6. B. S. Elkus, K. Abdelsalam, A. Rao, V. Velev, S. Fathpour, P. Kumar, and G. S. Kanter, "Generation of broadband correlated photon-pairs in short thin-film lithium-niobate waveguides," Opt. Express **27**, 38521 (2019).
7. J. Zhao, C. Ma, M. Rusing, and S. Mookherjea, "High quality entangled photon pair generation in periodically poled thin-film lithium niobate waveguides," Phys. Rev. Lett. **124**, 163603 (2020).
8. M. He, M. Xu, Y. Ren, J. Jian, Z. Ruan, Y. Xu, S. Gao, S. Sun, X. Wen, L. Zhou, L. Liu, C. Guo, H. Chen, S. Yu, L. Liu, and X. Cai, "High-performance hybrid silicon and lithium niobate Mach–Zehnder modulators for 100 Gbit s^{-1} and beyond," Nat. Photon. **13**, 359 (2019).
9. M. Zhang, C. Wang, R. Cheng, A. Shams-Ansari, and M. Lončar, "Monolithic ultra-high-Q lithium niobate microring resonator," Optica **4**, 1536 (2017).
10. R. Wu, J. Zhang, N. Yao, W. Fang, L. Qiao, Z. Chai, J. Lin, and Y. Cheng, "Lithium niobate micro-disk resonators of quality factors above 10^7," Opt. Lett. **43**, 4116 (2018).
11. R. Luo, H. Jiang, S. Rogers, H. Liang, Y. He, and Q. Lin, "On-chip second-harmonic generation and broadband parametric down-conversion in a lithium niobate microresonator," Opt. Express **25**, 24531 (2017).
12. H. Liang, R. Luo, Y. He, H. Jiang, and Q. Lin, "High-quality lithium niobate photonic crystal nanocavities," Optica **4**, 1251 (2017).
13. J. Lu, J. B. Surya, X. Liu, A. W. Bruch, Z. Gong, Y. Xu, and H. X. Tang, "Periodically poled thin-film lithium niobate microring resonators with a second-harmonic generation efficiency of 250,000/W," Optica **6**, 1455 (2019).
14. J. Y. Chen, Z. H. Ma, Y. M. Sua, Z. Li, C. Tang, and Y. P. Huang, "Ultra-efficient frequency conversion in quasi-phase-matched lithium niobate microrings," Optica **6**, 1244 (2019).
15. M. Zhang, B. Buscaino, C. Wang, A. Shams-Ansari, C. Reimer, R. Zhu, J. M. Kahn, and M. Lončar, "Broadband electro-optic frequency comb generation in a lithium niobate microring resonator," Nature **568**, 373 (2019).
16. C. Wang, M. Zhang, M. Yu, R. Zhu, H. Hu, and M. Lončar, "Monolithic lithium niobate photonic circuits for Kerr frequency comb generation and modulation," Nat. Commun. **10**, 978 (2019).
17. Y. He, Q. F. Yang, J. Ling, R. Luo, H. Liang, M. Li, B. Shen, H. Wang, K. Vahala, and Q. Lin, "Self-starting bi-chromatic $LiNbO_3$ soliton microcomb," Optica **6**, 1138 (2019).
18. J. Holzgrafe, N. Sinclair, D. Zhu, A. Shams-Ansari, M. Colangelo, Y. Hu, M. Zhang, K. K. Berggren, and M. Lončar, "Cavity electro-optics in thin-film lithium niobate for efficient microwave-to-optical transduction," Optica **7**, 1714 (2020).
19. T. P. McKenna, J. D. Witmer, R. N. Patel, W. Jiang, R. Van Laer, P. Arrangoiz-Arriola, E. A. Wollack, J. F. Herrmann, and A. H. Safavi-Naeini, "Cryogenic microwave-to-optical conversion using a triply resonant lithium-niobate-on-sapphire transducer," Optica **7**, 1737 (2020).
20. L. Shao, M. Yu, S. Maity, N. Sinclair, L. Zheng, C. Chia, A. Shams-Ansari, C. Wang, M. Zhang, K. Lai, and M. Lončar, "Microwave-to-optical conversion using lithium niobate thin-film acoustic resonators," Optica **6**, 1498 (2019).
21. Z. Yu and X. Sun, "Acousto-optic modulation of photonic bound state in the continuum," Light Sci. Appl. **9**, 1 (2020).
22. Y. Hu, M. Yu, D. Zhu, N. Sinclair, A. Shams-Ansari, L. Shao, J. Holzgrafe, E. Puma, M. Zhang, and M. Lončar, "Reconfigurable electro-optic frequency shifter," arXiv:2005.09621 (2020).

23. C. Wang, M. Zhang, B. Stern, M. Lipson, and M. Lončar, "Nanophotonic lithium niobate electro-optic modulators," Opt. Express **26**, 1547 (2018).
24. K. Luke, P. Kharel, C. Reimer, L. He, M. Lončar, and M. Zhang, "Wafer-scale low-loss lithium niobate photonic integrated circuits," Opt. Express **28**, 24452 (2020).
25. J. Zhang, Z. Fang, J. Lin, J. Zhou, M. Wang, R. Wu, R. Gao, and Y. Cheng, "Fabrication of crystalline microresonators of high quality factors with a controllable wedge angle on lithium niobate on insulator," Nanomaterials **9**, 1218 (2019).
26. R. Gao, H. Zhang, F. Bo, W. Fang, Z. Hao, N. Yao, J. Lin, J. Guan, L. Deng, M. Wang, L. Qiao, and Y. Cheng, "Ultrahigh quality-factor microresonators fabricated in pristine lithium niobate thin film for efficient nonlinear optics applications," arXiv:2102.00399 (2021).
27. D. Berkoh and S. Kulkarni, "Challenges in lift-off process using camp negative photoresist in III–V IC fabrication," IEEE Trans. Semicond. Manuf. **32**, 513 (2019).
28. Y. Liu, H. Li, J. Liu, S. Tan, Q. Lu, and W. Guo, "Low V_π thin-film lithium niobate modulator fabricated with photolithography," Opt. Express **29**, 6320 (2021).
29. R. Wolf, I. Breunig, H. Zappe, and K. Buse, "Scattering-loss reduction of ridge waveguides by sidewall polishing," Opt. Express **26**, 19815 (2018).
30. S. Y. Siew, E. J. H. Cheung, H. Liang, A. Bettiol, N. Toyoda, B. Alshehri, E. Dogheche, and A. J. Danner, "Ultra-low loss ridge waveguides on lithium niobate via argon ion milling and gas clustered ion beam smoothening," Opt. Express **26**, 4421 (2018).